Review

Medical imaging of pulmonary disease in SARS-CoV-2-exposed non-human primates

Marieke A. Stammes [ID], [1,*] Ji Hyun Lee, [2] Lisette Meijer, [1] Thibaut Naninck, [5] Lara A. Doyle-Meyers, [6,7] Alexander G. White, [3] H. Jacob Borish, [3] Amy L. Hartman, [4,8] Xavier Alvarez, [9] Shashank Ganatra, [9] Deepak Kaushal, [9] Rudolf P. Bohm, [6,7] Roger le Grand, [5] Charles A. Scanga, [3,4] Jan A.M. Langermans, [1,10] Ronald E. Bontrop, [1,11] Courtney L. Finch, [2] JoAnne L. Flynn, [3,4] Claudia Calcagno, [2] Ian Crozier, [12] and Jens H. Kuhn [2]

Chest X-ray (CXR), computed tomography (CT), and positron emission tomography–computed tomography (PET-CT) are noninvasive imaging techniques widely used in human and veterinary pulmonary research and medicine. These techniques have recently been applied in studies of severe acute respiratory syndrome coronavirus 2 (SARS-CoV-2)-exposed non-human primates (NHPs) to complement virological assessments with meaningful translational readouts of lung disease. Our review of the literature indicates that medical imaging of SARS-CoV-2-exposed NHPs enables high-resolution qualitative and quantitative characterization of disease otherwise clinically invisible and potentially provides user-independent and unbiased evaluation of medical countermeasures (MCMs). However, we also found high variability in image acquisition and analysis protocols among studies. These findings uncover an urgent need to improve standardization and ensure direct comparability across studies.

The role of medical imaging in the assessment of coronavirus disease 2019 in humans and NHPs

A hallmark of coronavirus disease 2019 (COVID-19) is lower respiratory tract infection and viral-induced pneumonia in most hospitalized patients [1]. In humans, parenchymal lung involvement in COVID-19 is typically evaluated using medical imaging, most commonly **CXR** (see Glossary) and **CT**. A spectrum of lung imaging features characteristic of COVID-19 has now been established, including alveolar, interstitial, pleural, and vascular abnormalities. Most found COVID-19 abnormalities are alveolar **ground glass opacities (GGOs)**, often with interlobular and intralobular septal interstitial thickening (crazy-paving pattern) in a bilateral, multilobar, and peripheral distribution [1,2]. In patients, these readouts have been found to uniquely complement real-time reverse transcription qPCR (RT-qPCR) measurements of SARS-CoV-2 loads and to aid the evaluation of COVID-19 progression and severity [3]. However, the host–virus determinants of parenchymal pulmonary disease and radiographic pulmonary abnormalities in the pathogenesis of COVID-19 remain unclear. Specifically, a clear understanding of the relationship between upper or lower respiratory tract viral loads and pulmonary immunopathology is lacking. These shortcomings arise, at least partially, because collecting serial imaging data that can be rigorously mapped to clinical, virological, and immunological markers is an operational challenge in the clinical setting, frequently limited by the absence of baseline pre-infection lung imaging.

Noninvasive, longitudinal imaging of established animal models of SARS-CoV-2 infection and COVID-19 may allow more effective delineation of the pathogenesis of lung disease *in vivo* in controlled experimental settings. NHPs are arguably well suited as animal models of COVID-19

Highlights

In non-human primates (NHPs), characteristic radiographic abnormalities (best observed by high-resolution imaging), combined with concordant immunological, virological, and lung histopathological findings, mirror mild-to-moderate human disease.

Noninvasive medical imaging can visualize otherwise 'silent' disease at high resolution and generates quantifiable measurements that are particularly important in sublethal models, providing an essential complement to standard immunological, virological, and pathological assays, which can only be performed as snapshots (not longitudinally) or may be difficult to perform.

The incorporation of advanced medical imaging tools in NHP studies for coronavirus disease 2019 (COVID-19) research is not without challenges, including high experimental costs due to the limited availability of equipment in high containment environments, frequency of anesthesia events required for imaging, and the number of animals that can practically be imaged at a single time point.

[1]Biomedical Primate Research Centre (BPRC), 2288 GJ, Rijswijk, The Netherlands
[2]Integrated Research Facility at Fort Detrick (IRF-Frederick), Division of Clinical Research (DCR), National Institute of Allergy and Infectious Diseases (NIAID), National Institutes of Health (NIH), Fort Detrick, Frederick, MD 21702, USA
[3]Department of Microbiology and Molecular Genetics, School of Medicine, University of Pittsburgh, Pittsburgh, PA 15213, USA

due to their overall close evolutionary relationship to humans and the consequent physiological similarities [4], including elicited host immune responses and systemic distribution of angiotensin-converting enzyme 2 (ACE2), the cellular receptor of SARS-CoV-2 [5]. Some of the typical manifestations of SARS-CoV-2 infection in humans (i.e., asymptomatic, subclinical, infection, or mild disease) are modeled successfully in NHPs (see Clinician's corner and Box 1) [6,7].

During the COVID-19 pandemic, medical imaging with CXR, CT, and **PET-CT** has been applied to characterize lung involvement in SARS-CoV-2-exposed NHPs, for which it has proven a meaningful, noninvasive complement to standard virological assessments. Serial imaging (including pre-exposure baselines) enables longitudinal data collection through frequent examination of each animal and uses a limited number of animals [8,9]. In addition, because the animals are imaged using the same modalities and scanners used to examine patients, readouts of SARS-CoV-2-exposed NHPs are highly translational. However, as is the case with other viral pathogens, imaging of SARS-CoV-2 infection in NHPs has suffered from a lack of standardization across different laboratories, impacting image acquisition, analysis, and, ultimately, reported imaging metrics. Efforts to harmonize imaging approaches in the setting of SARS-CoV-2/COVID-19 modeling are urgently needed.

In this review, we provide a summary of noninvasive imaging studies in NHP COVID-19 models completed thus far. We identify current challenges and future needs in this arena and offer guidance to enhance future imaging studies of SARS-CoV-2 exposure and disease progression in NHPs.

An in-depth look at the role of CXR, CT, and PET-CT in the evaluation of COVID-19

Diagnostic confirmation of SARS-CoV-2 infection/COVID-19 requires virus-specific nucleic acid amplification (e.g., RT-PCR) or antigen detection, and chest imaging is not recommended for

[4]Center for Vaccine Research, School of Medicine, University of Pittsburgh, Pittsburgh, PA 15213, USA
[5]Center for Immunology of Viral, Auto-immune, Hematological and Bacterial diseases (IMVA-HB/IDMIT), Université Paris-Saclay, Inserm, CEA, 92260 Fontenay-aux-Roses, France
[6]Tulane National Primate Research Center, Covington, LA 70433, USA
[7]Department of Medicine, Tulane University School of Medicine, New Orleans, LA 70112, USA
[8]Department of Infectious Diseases and Microbiology, School of Public Health, University of Pittsburgh, Pitt Public Health, Pittsburgh, PA 15261, USA
[9]Texas Biomedical Research Institute, San Antonio, TX 78227, USA
[10]Department Population Health Sciences, Division of Animals in Science and Society, Faculty of Veterinary Medicine, Utrecht University, 3584 CL, Utrecht, The Netherlands
[11]Department of Biology, Theoretical Biology and Bioinformatics, Utrecht University, 3584 CH, Utrecht, The Netherlands
[12]Clinical Monitoring Research Program Directorate, Frederick National Laboratory for Cancer Research, Frederick, MD 21701, USA

*Correspondence:
stammes@bprc.nl (M.A. Stammes).

Box 1. Similarities and differences in phenotype of symptomatic SARS-CoV-2 infection in NHPs versus humans

The aim of experimental animal models is to understand infection and disease to enable effective prevention or treatment. Studies in NHPs have explored the natural history of infection and disease, including viral dynamics, host immune responses, and host pathology. NHP models have been used to evaluate vaccine and therapeutic countermeasures. Evaluation of these results requires an understanding of how well (or not) the NHP models SARS-CoV-2 infection and COVID-19 in humans [58].

The clinical manifestations of SARS-CoV-2 infection observed in current NHP models are variably present but have included fever, weight loss, loss of appetite, pale appearance, dehydration, diarrhea, and nasal discharge. These signs are comparable with the spectrum of clinical symptoms detected in humans with mild disease. In most NHP studies, and similar to humans with mild disease, no clinical differences were consistently observed between males and females or young and old macaques. In addition, severe and critical disease, though reported in a few aged NHPs, has not been observed reliably [34].

In NHPs, viral replication was mainly observed in the respiratory tract (nasal cavity, oropharynx, and lungs) and gastrointestinal system. At necropsy, lungs showed mild-to-moderate interstitial pneumonia and swollen lymph nodes. In humans, viral replication is most prominently detected in the upper respiratory epithelia and may be found in other parts of the body [101]; in addition to severe respiratory failure, human autopsy data show systemic involvement of multiple organ systems, including cardiovascular, renal, and neurologic, but apart from the respiratory tract, it is challenging to describe morphological alterations attributable to SARS-CoV-2 infection [102]. Innate and adaptive immune responses to SARS-CoV-2 infection paralleled those observed in humans, including adaptive humoral [e.g., anti-SARS-CoV-2 nucleocapsid (N) and spike (S) IgG antibodies] and cellular (e.g., antigen-specific T cell) responses. After infection, innate and adaptive cytokine/chemokine production in NHPs also mirrors human responses, though the dysregulated cytokine storm described in humans with severe disease has not been observed in NHPs.

In short, current NHP models of COVID-19 [rhesus monkeys, crab-eating (cynomolgus) macaques, grivets/vervets, and common marmosets] recapitulate mild-to-moderate disease in humans in both clinical and radiological presentation; severe and fatal disease has not yet been effectively modeled [8,18–20,31,39,58,103–107].

routine screening and diagnosis or in patients with mild symptoms or without symptoms [1,10,11]. However, chest imaging may complement the initial evaluation to inform management in patients with lower respiratory symptoms and signs and/or in patients with worsening respiratory status as the clinical syndrome evolves and/or in patients with potential alternative diagnoses. When indicated, CXR and CT are predominantly used. CXR is a fast, relatively inexpensive, portable, and widely available imaging technique frequently used in clinical settings [9,12–35]. Particularly early during the course of infection, and especially in patients with mild disease, the sensitivity of CXR compared with RT-PCR is relatively low, at only 69% [although the overall **positive predictive value (PPV)** remains high at 95.7%] [1,3,36–41]. By contrast, multiple studies and meta-analyses have shown chest CT to be more sensitive (94% versus 89% for RT-PCR [42]), although at a recognized cost of specificity, which is dependent on local prevalence and pretest probability [42]. Notably, chest CT has been able to identify patients with COVID-19 even when RT-PCR testing was negative early during disease progression [43]. The emerging evidence base regarding the use of CXR and CT imaging in COVID-19 has led to consensus guidelines that detail relative strengths and weaknesses and provide recommendations [1,10,11]. These sensitivity limitations also apply to imaging of SARS-CoV-2-exposed NHPs, and CXR has been widely used in research studies. Although most human CXR examinations are inconclusive during the early stages of COVID-19 [37], 28 studies of SARS-CoV-2-exposed NHPs detected CXR abnormalities early after exposure [9,13–17,20–23,26,27,29,32,35,44–46]. However, CXR imaging was inconclusive in other studies [12,13,23–25,28] and was generally found to be uncorrelated with the degree of lung abnormalities at necropsy (Figure 1).

Although consensus guidelines [1,10,11] have not clearly defined the relative merits of CXR versus CT imaging in assessing COVID-19, chest CT is recommended for the evaluation of patients with COVID-19, typically to inform clinical management in patients who are severely ill or deteriorating, including the exclusion of other diagnoses, such as pulmonary embolism. CT imaging has been applied in 16 published studies of SARS-CoV-2-exposed NHPs (Table 1) [47]. As a tomographic imaging modality that acquires data in 3D and at higher resolution compared with CXR, chest CT is more sensitive and affords more detailed qualitative and quantitative characterization of lung abnormalities [38]. The risks and benefits associated with chest CT versus CXR are only partly applicable to NHPs in a research setting: higher radiation exposure has less consequence because most studies are terminal; staff in contact with research animals are always in biosecure personal protective equipment; and potential contamination of imaging suites is mitigated by scheduled rigorous decontamination [1,48].

In NHP studies, CT imaging generally mirrored imaging of human lung abnormalities both in character and distribution. The reported prevalence of common CT findings in SARS-CoV-2-exposed NHPs is shown in Table 1 and Figure 2. Compared with human disease, CT abnormalities (most commonly GGOs) in NHPs were detected at a much earlier disease stage and resolved fairly rapidly, albeit with considerable intersubject heterogeneity; most abnormalities were first observed starting at 2 days post-exposure and resolved within 2 weeks [33].

CXR and chest CT are mainly anatomical imaging modalities that provide structural characterization (i.e., the location, volume, morphology, and texture of lung abnormalities). By contrast, PET-CT combines the high-resolution anatomical information from CT with quantitative functional assessments by PET. When performed with the metabolic radiotracer [fluorine-18]fluoro-2-deoxyglucose (^{18}F-FDG), a glucose analog that is internalized but not metabolized by metabolically active inflammatory cells], PET-CT enabled the quantification of heightened metabolic activity as a proxy of inflammation in lung parenchyma, regional lymph nodes, heart, kidneys, bone marrow, brain, and other organs in the context of COVID-19 [8,9,49–51]. However, its limited availability in many

Glossary

Acute respiratory distress syndrome (ARDS): an acute, diffuse, inflammatory injury to the lungs that is associated with a variety of etiologies, including infections, and is associated with high case fatality.

Bronchoalveolar lavage (BAL): used to collect a sample from the lungs, a bronchoscope is used to instill saline solution and then the fluid is collected.

Chest X-ray (CXR): exposure of lungs to ionizing radiation to produce pictures used to diagnose and monitor lung conditions.

Computed tomography (CT): several X-ray scans from numerous angles are processed by a computer to create cross-sectional images, referred to as 'slices'.

Dual-energy CT (DECT): a recently developed CT technology that combines two separate X-ray sources with different spectra to produce CT images at different energy levels.

DOTATATE: a peptide specific for SSTR2 receptors, which are expressed on certain kinds of inflammatory cells. When labeled with gallium-68 or copper-64, this peptide can be used as a tracer for PET imaging.

Ground glass opacity (GGO): abnormalities seen on chest X-rays and CT imaging of lungs. They present as hazy areas that indicate increased density.

Half-maximum infection dose (ID$_{50}$): the estimated number of organisms or virus particles required to produce infection in 50% of normal subjects when exposed by a given route.

Magnetic resonance imaging (MRI): MRI scanners use computer-generated radio waves and a magnetic field to create detailed images of organs and tissues.

Percent change in lung hyperdensity (PCLH): to quantify lung abnormalities, the lung volume involved in pneumonia is identified above a 'hyperdensity' threshold and then tracked by comparing the same region of interest over time.

Positron emission tomography (PET): diagnostic imaging test that uses radioactive tracers to show functional activity of body tissue cells through 3D mapping. Different tracers are used for different targets.

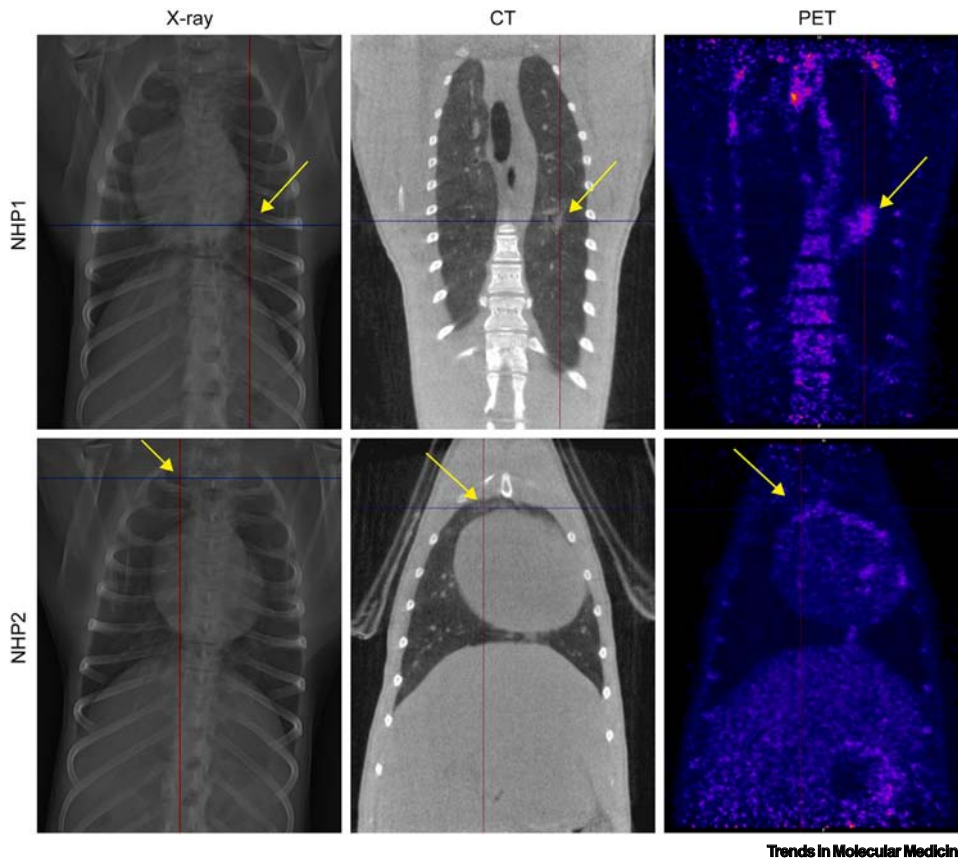**Positive predictive value (PPV):** when screening patients, this is the

Figure 1. Comparison of chest X-ray (CXR), computed tomography (CT), and positron emission tomography–computed tomography (PET-CT) imaging. To compare results in non-human primate (NHP) lungs after severe acute respiratory syndrome coronavirus 2 (SARS-CoV-2) exposure, images on the same row originate from the same animal and were obtained on the same day (day 4 post-exposure). For the animal in the upper row, the lesion located in the middle part of the left lung (marked by the crosshairs and arrows) is clearly visible using all three imaging modalities. By contrast, alterations in lung density for the animal shown in the bottom row could only be clearly distinguished from healthy lung using CT (marked by the crosshairs and arrows) but are hardly visible on CXR and PET-CT. Adapted from [9].

proportion of positive results in statistics and diagnostic tests that are true positives.

Translocator protein (TSPO): transmembrane protein located on the outer mitochondria membrane and mainly expressed in glial cells in the brain and on activated macrophages.

Somatostatin receptor 2 (SSTR2): protein-coding gene acting as a general inhibitor of the release of hormones and secretory proteins in the cerebrum and kidneys.

Standard uptake value (SUV): a way of determining activity in PET. Computer software converts the visual data into numerical values for the measured activity, normalized for body weight/surface area, and injected dose.

countries and emergency settings has restricted its application as a frontline COVID-19 diagnostic imaging modality in the clinic. In preclinical research settings, PET-CT is being increasingly used in NHP studies to evaluate human respiratory diseases, most notably tuberculosis [52]. However, even in preclinical settings, this imaging modality is not widely available in biocontainment laboratories; PET-CT imaging has been used in only six studies of SARS-CoV-2-exposed NHPs (Table 1 and Figure 1) [8,9,34,49–51]. Other imaging modalities can be applied in both humans and NHPs for diagnosis of COVID-19 (Box 2).

Qualitative and quantitative analysis of COVID-19-related lung abnormalities detected by CT and PET-CT

Reliable quantification of lung abnormalities identified by *in vivo* imaging within (and among) experimental NHP groups is of great interest to allow meaningful correlations with histopathological data and for the evaluation of both therapeutic and prophylactic treatment efficacy [8,33,35,49,53,54]. Although data continue to accumulate, COVID-19-related lung abnormalities detected by CT have already been successfully matched with gross pathology of NHP samples (Figure 3). Several semiquantitative scoring systems based on lesion volume and type

Table 1. Summary of SARS-CoV-2 studies in NHPs meeting inclusion criteria[a]

Animal				Exposure			Imaging method			Imaging results		Refs
Type	Number and sex	Age (y)	Weight (kg)	SARS-CoV-2 isolate	Dose and volume	Inoculation route	Modality	Frequency	Analysis method	Lesion type	Time	
'African green monkey'	6 (4 f + 2 m)	Adult	NA	P3 INMI1/2020/Italy	4.6×10^5 PFU (6 ml)	Intratracheal + intranasal	CXR	D1, D2, D3, D4, D5	Radiologists interpret + veterinarian/veterinary pathologist	Did not reflect degree of lesions and hemorrhage of lungs seen at necropsy	Inconclusive	[12]
	8 (4 m + 4 f)	NA	3.5–6	P4 USA_WA1/2020	1.82×10^6 PFU (6.5 ml)	Intranasal (1 ml) + intratracheal (4 ml) + oral (1 ml) + ocular (0.5 ml)	CXR	Pre-infection, D1, D3, D5, D7, D10	NA	NA	NA	[13]
	11	NA	3.8–6.7	P3 SARS-CoV-2/human/USA/RML-7/2020 (MW127503.1), 16 strain D614G or P3 hCoV-19 19/England/204820464/2020, EPI_ISL_683466	1.0×10^6 PFU (1 ml)	Intranasal	CXR	Pre-infection, D1, D3, D5, D7	CXR score	Pulmonary infiltrates	D1–D7	[14]
'African green monkeys'/crab-eating macaques	AGM: 14 (m) CEM: 4 (2 m + 2 f)	4.2–8	AGM: 5.6–7.55 CEM: 2.3–3.9	USA_WA1/2020	NA	Intratracheal + intranasal	CXR of AGM	D3, D7	NA	Focal interstitial pattern, mild bronchial pattern (n = 2), enlarged tracheobronchial lymph nodes (n = 1)	D3–D7	[15][b]
Rhesus monkeys	8 (m + f)	4–6	NA	P3 nCoV-WA1-2020	1.82×10^6 PFU (6.5 ml)	Intratracheal, intranasal, oral, ocular	CXR	Pre-infection, D1, D3, D5, D7, D10, D12, D14, D17, D21	Clinical veterinarian interpretation	Mild-to-moderate pulmonary infiltrates	D1–D12	[16]
	6 (m + f) (+2 mock)	6–11	5–12	BetaCoV/Wuhan/WIV04/2019	4.9×10^6 PFU (1 ml)	Intratracheal	CXR	Pre-infection, D1, D3, D6	NA	Patchy GGOs	D1–D6	[17]
	4 (+2 re-exposure control, +1 mock)	3–5	3–5	WH-09/human/2020/CHN isolated in their laboratory	0.7×10^6 PFU (1 ml) for both exposures	Intratracheal (n = 6), re-exposure: intratracheal on D28 (= 0 dpr) (n = 4)	CXR	Pre-infection, D7, D28, D33 (= 5 dpr)	Radiological interpretation	Bilateral GGOs, pneumonia	D7	[18]
	5	3–5 (n = 3), 15 (n = 2)	NA	Unspecified	0.7×10^6 PFU (1 ml)	Intratracheal	CXR	Pre-infection, D5, D6, D7, D8, D9, D11, D13, D15	NA	Interstitial infiltration	D5 old; D7 young	[19]

Table 1. (continued)

Animal				Exposure			Imaging method			Imaging results		Refs
Type	Number and sex	Age (y)	Weight (kg)	SARS-CoV-2 isolate	Dose and volume	Inoculation route	Modality	Frequency	Analysis method	Lesion type	Time	
	12 (m + f)		3.6–5.7	P3 nCoV-WA1-2020	1.1×10^7 PFU (6 ml)	Intranasal, oral, ocular, intratracheal	CXR	Pre-infection, D1, D3, D5, D7	Clinical veterinarian interpretation	Lobe involvement, pulmonary infiltration	D1–D7	[20]
	5 (m)	3–5	NA	WH-09/human/2020/CHN	0.7×10^6 PFU	Conjunctival ($n = 2$) or intratracheal ($n = 1$) or intragastrical ($n = 2$)	CXR	Pre-infection, D1, D3, D5, D7	NA	Interstitial infiltration, costophrenic angles, patchy lesions	D3–D7	[21]
	8 (m + f)	11–17	NA	2019-nCoV/USA-WA1/2020	1.1×10^6 PFU (2 ml)	Intranasal + intratracheal	CXR	D5, D2, D4, D7, D10	Radiological interpretation, radiograph score	Pulmonary infiltration, GGOs for 2/4 untreated group, 0/4 treated group, 1/4 untreated group – severe pneumonia	D2–D10	[22]
	16 (f)	3.5–10	4.5–10	P3 nCoV-WA1-2020	2.8×10^5 PFU (6.5 ml)	Intratracheal (4 ml), intranasal (1 ml), oral (1 ml), ocular (0.5 ml)	CXR	Pre-infection, D1, D3, D5, D7	Lung radiography score	NA	D1–D7	[23][b]
	12 (m + f)	3–11	4–10	Unspecified	0.7×10^6 PFU (5 ml)	Intrabronchial (4 ml) + intranasal (1 ml)	CXR	D28, D27, D25, D-21, D14, D7, D0, D1, D3, D5, D7	NA	Mild, no evidence of frank consolidative pneumonia	NA	[24]
	5	6–7	NA	BetaCoV/Wuhan/WIV04/2019	0.7×10^5 PFU	Intratracheal	CXR	Pre-infection, D3, D6	NA	NA	NA	[25]
	10 + 1 (mock) (m)	NA	NA	From CDC Guangdong Province, China	1×10^7 PFU (1 ml)	Intragastric by gavage and intranasal	CXR	Pre-infection, D1, D4, D7, D14	NA	Nodular lesions caused by pulmonary infiltrates	D4–D7	[26]
	12 (6 m + 6 f)	3.5–6.5	5.82–12.81	USA_WA1/2020	2.5×10^6 PFU (2.5 ml)	Intratracheal (2 ml) + intranasal (0.5 ml)	CXR	Pre-infection, D1, D3, D5, D7	Veterinary radiologists CXR score	Pulmonary infiltrates	D3–D7	[27][b]
	44 (m)	3.5–8	NA	USA_WA1/2020	1.0×10^6 PFU (1.01 ml)	Intratracheal (0.5 ml) + intranasal (0.5 ml) + ocular (0.01 ml)	CXR	D6, D13, D20	CXR score	Subtle radiographic changes	D6–D20	[28][b]

Animal	Number	Age	Weight	Virus strain	Dose	Route	Imaging	Imaging timepoints	CXR score	Pulmonary findings	Findings timepoint	Refs
Crab-eating macaques	16 (m + f)	3–5 (m), 16–23 (m + f)	± 5, ± 9–15	P4 USA_WA1/2020	1.82×10^6 PFU (6.5 ml)	Intratracheal (4 ml) + intranasal (1 ml) + ocular (1 ml) + ocular (0.5 ml)	CXR	Pre-infection, D1, D3, D5, D7, D10, D14, D17, D21	CXR score by clinical veterinarian	Pulmonary infiltrates	D1–D21	[29][b]
Pigtail macaques	2 + 4 (mock + vaccinated) (f)	7–10	NA	Unspecified	2×10^7 PFU (7 ml HBSS)	Conjunctival, intranasal, oral cavity, intratracheal	CXR	Pre-infection, D1, D3, D5, D7	NA	Mock, pneumonia; vaccinated, no lesion	D1–D7	[46][b]
	4 (m)	5.64–6.07	5.8–8.6	USA_WA1/2020	0.7×10^6 PFU	Intratracheal + intranasal	CXR	Pre-infection, D6, D14, D21	NA	Interstitial pneumonia	NA	[30][b]
Crab-eating macaques/ rhesus monkeys/ common marmosets	CEM: 6; RM: 14 (m + f); CM: 6 (m + f)	RM: 1, (n = 4), 5 (n = 6) 13–18 (n = 4); CEM: 5–6; CM: 6 adults	NA	From CDC Guangdong Province, China	Adult RM + CEM 4.75×10^6 PFU (4.75 ml); half-dose child RM; CM: 1.0×10^6 PFU (1 ml)	Intratracheal, intranasal, ocular	CXR	Pre-infection, D2, D4, D6, D8, D10, D12, D14, D17, D21	Radiologist interpretation	Interstitial areas and nodules/ masses	D12	[31]
'African green monkeys/ crab-eating macaques/ rhesus monkeys	AGM: 3; CEM: 4; RM: 4 (m + f)	Adult	NA	nCoV-WA1-2020 (R4717)	3.84×10^4 PFU (mean inhaled)	Aerosol (1–3 μm MMAD)	CXR	D1, D3, D5, D7, D9, D11, D15, D18	NA	Increased lung opacity and presence of infiltrates	D3–D11	[32]
Rhesus monkeys/ crab-eating macaques	RM: 7 (m + f); CEM: 1 (f)	RM: 3.8–4; CEM: 7	NA	USA_WA1/2020	1.5×10^8 TCID$_{50}$	Mucosal atomization (1 ml) + intratracheal (4 ml)	CXR	Control: pre-infection, D2, D3, D4, D5, D7, D10, D14, D21; vaccinated: pre-infection, D2, D4, D6, D8	NA	Control: infiltrates, GGOs, consolidation, crazy-paving pattern, linear opacities; vaccinated: lacked abnormalities	D2–D5	[45]
	RM: 8 (m + f); CEM: 8 (m + f)	5.3–9.8	2.98–9.59	USA_WA1/2020	RM: 5.85×10^4 PFU; CEM: 6.66×10^4 PFU; 2.65×10^7 PFU	Aerosol (n = 8); intratracheal/ intranasal (n = 8)	CXR	D28, D20/19, D2, D4, D6, D8, D9, D10	NA	Infiltrates, opacities	D2–D8; (peak: D4–D6)	[44][b]
Rhesus monkeys	12 (m + f)	2–4	3.73–5.52	P3 Victoria/01/2020	5×10^6 PFU (3 ml)	Intranasal (1 ml) and intratracheal (2 ml)	CT	Pre-infection, D5	Medical radiologist; COVID pattern score and zone score	Predominantly bilateral disease, GGOs, consolidation	D5, n = 3/6 vaccinated and n = 5/6 unvaccinated	[57]

Table 1. (continued)

Animal				Exposure			Imaging method			Analysis method	Imaging results		Refs
Type	Number and sex	Age (y)	Weight (kg)	SARS-CoV-2 isolate	Dose and volume	Inoculation route	Modality	Frequency			Lesion type	Time	
	18 (m + f)	3–6	>4.5	P3 Victoria/01/2020	5 × 10^6 PFU (3 ml)	Intranasal (1 ml) and intratracheal (just above carina, 2 ml)	CT	Pre-infection, D5		CT score	Relatively mild and only affected less than 25% of lung	D5, $n = 3/6$ vaccinated high dose, $n = 6/6$ vaccinated low dose, $n = 5/6$ unvaccinated	[54]b
	18 (9 m + 9 f)	2.5–3.5	>4	P3 Victoria/01/2020	5.0 × 10^6 PFU (3 ml)	Intratracheal (2 ml) + intranasal (1 ml)	CT	Pre-infection, D5		CT score by medical radiologist	COVID pattern score + zone score	D5	[73]
Crab-eating macaques	39 (m + f)	3	2.85–4.62	P5 hCoV-19/France/IDF0372/2020	1.0 × 10^6 PFU (4.5 ml)	Intranasal + intratracheal (just above carina)	CT	Pre-infection, D2, D5, D11/13		CT score (lesions scored based on type and area involved)	GGOs, crazy-paving pattern, consolidation, pleural thickening	D2–D11/13	[56]
	10 (f)	3–6	NA	BetaCoV/France/IDF/0372/2020	1 × 10^6 PFU (4.5 ml)	Intranasal + intratracheal	CT	D3		CT score, including lesion type and volume by two people	Small lung lesions, GGOs	D3 is N9/10 positive	[53]
	8	NA	NA	hCoV-19/France/IDF0372/2020	1.0 × 10^5 PFU (5 ml)	Intratracheal (4.5 ml) + intranasal (0.5 ml)	CT	D3, D7, D10, D14		CT score including lesion type and volume	Nonextended GGOs	D3–D14	[74]b
	10 (3 m+7 f)	3–8 ($n = 5$), 23–30 ($n = 5$)	2.3–6.0	Unspecified	0.7 × 10^6 PFU + RE 0.7 × 10^6 PFU ($n = 2$)/0.7 × 10^5 PFU ($n = 2$)	Intratracheal (0.9/1.0 ml) + intranasal (0.1 ml), RE: intratracheal	CT (slice of third, sixth, ninth thoracic vertebrae used)	CT: pre-infection, (D3), D5, (D7), D10, (D12, D14) RE: D0, D2, D7 ($n = 3$)		Visual interpretation	Pneumonia	D3–10/12	[66]
Crab-eating macaques/rhesus monkeys	12 (m + f)	2–4	2.89–4.85	P3 Victoria/01/2020	5.0 × 10^6 PFU (3 ml)	Intranasal + intratracheal just above carina	CT ($n = 4$)	D18		Radiologist interpretation	GGOs, pulmonary abnormalities and peripheral consolidations that involved <25% of lung	D18	[65]
Rhesus monkeys	28 (+5 mock) (m)	3–9	4.6–11.7	USA WA1/2020	3.2 × 10^6 PFU	Intranasal + intratracheal	PET-CT ($n = 6$)	Pre-infection and D4/5		Whole-lung uptake, ROI based on SUV >1.5 SUVCMR	No vaccine-associated enhanced respiratory disease found	NA	[122]

Species	n	Age	Weight (kg)	Virus strain	Dose	Route	Imaging	Imaging time points	Analysis	Findings	Finding time points	Refs
Hamadryas baboons/ rhesus monkeys/ common marmosets	HB: 12 RM: 16; CM: 6; Study 1: 4 RM; Study 2: 6 RM (m + f)	HB: 2–20; RM: 3–22; CM: 6–7	HB: 5.6–27.5; RM: 4.2–10.2; CM: 0.35–0.56	P6 USA-WA1/2020	1.05×10^6 PFU (0.5 ml HB + RM); 8.82×10^5 PFU (0.42 ml CM)	Ocular, intranasal, intratracheal	CXR, CT (CBCT)	Study 1: CT: pre-infection, D1, D2, D3; Study 2: CT: D6, D12	CXR: veterinary clinician score CT: PCLH + score	GGOs, crazy-paving pattern, pneumonia	Study 1: D1–D3; Study 2: D6, D12	[33]
Rhesus monkeys	21 (m) [+6 (m) mock]	2–4	NA	P6 USA-WA1/2020	1.05×10^3 PFU (0.5 ml)	Intranasal (0.25 ml) and intratracheal (0.25 ml)	CXR, CT (CBCT)	Various schedules with D4/5 CXRs; pre-infection, D1, D3, D6, D10/EOP; CT: pre-infection, D3/4, EOP	Veterinary radiological interpretation (2), CT score	Generally minimal or mild, not consistently associated with viral challenge	All time points	[35]
Crab-eating macaques	3 (+3 mock) (m + f)	4–4.5	3.17–4.62	2019-nCoV/ USA-WA1-A12/ 2020	3.65×10^6 PFU (4 ml)	Direct bilateral primary post-carinal intrabronchial instillation	CT; PET-CT	CT: pre-infection, D2, D4, D6, D8, D10, D12, D19, D30 PET-CT: pre-study, D2, D6, D12	CT: PCLH, score, radiologist interpretation PET: SUV_{max}	GGOs, consolidations, interlobular septal thickening	D2–D12	[8][b]
	12 (5 m + 7 f)	3.6–3.8		hCoV-19/France/ IDF0372/2020	1.0×10^5 PFU (5 ml)	Intratracheal (4.5 ml) + intranasal (0.5 ml)	CT, PET-CT	CT: pre-infection, D5/6, D14; PET-CT: pre-infection, D5/6	CT score including lesion type and volume; PET: SUV_{mean}	GGOs, crazy-paving pattern, consolidation, lung draining lymph node activation	D5–14	[51]
Crab-eating macaques/ rhesus monkeys	8 (m)	4–6 + 16 (CEM)	3.3–9.7	P5 BetaCoV/ BavPat1/2020	0.7×10^5 PFU (5 ml)	Intratracheal (upper part, 4.5 ml) and intranasal (0.25 ml per nostril)	CT (gated) (CBCT); PET-CT	CT: pre-infection, D2, D4, D6, D8, D10, D12, D14, D16, D22 PET-CT: D8, D16, D22, D29, D35	CT: CT score PET-CT: LN volume, LN HU density, LN SUV_{mean}, SUV_{peak}	GGOs, consolidations, crazy-paving pattern; SUVs on lymph nodes; one showed left ocular region	D2–D35	[49]
'African green monkeys'/ rhesus monkeys	AGM: 4 (2 m + 2 f); RM: 4 (3 m + 1 f)	AGM: ≈16; RM: 13–15	AGM: 3.5–7.4; RM: 7.5–16.0	USA-WA1/2020	1.4×10^3 PFU (aerosol, n = 4); 3.61×10^6 PFU (N=4)	Aerosol (≈2 µm MMAD) (2AGM + 2RM); multiple routes (oral, 1 ml; nasal, 1 ml; intratracheal, 1 ml; conjunctival, 50 µL per	CXR PET-CT performed, not included	D7, D7, D14, D21; +AGM1 on D8; + AGM2 on D22	Radiological interpretation	Diffuse alveolar pattern, mild alveolar pattern, radiographic opacities	D7–D8; D21–D22	[34]

Table 1. (continued)

Animal				Exposure			Imaging method		Imaging results			Refs
Type	Number and sex	Age (y)	Weight (kg)	SARS-CoV-2 isolate	Dose and volume	Inoculation route	Modality	Frequency	Analysis method	Lesion type	Time	
						eye).						
Rhesus monkeys	28 (f)	4–8	5.4–12.1	P4 BetaCoV/ German/ BavPat1/2020	0.7×10^5 PFU (5 ml)	Intratracheal (4.5 ml) + intranasal (0.5 ml)	CT (gated) (CBCT), LUS	Pre-infection, D2, D7, D14	CT score, LUS score	CT: GGOs, consolidations, crazy paving patterns LUS: B-lines with or without pleural abnormalities	D2–14	[67]
'African green monkeys'	4 (+2 mock) (m)	3.5	4.2–6.3	P3 München-1.1/2020/929 (Munich) virus	$1.0 \times 10^{3.7–4.2}$ (aerosol); 2.5×10^6 PFU (5 ml)	Aerosol (1.7 μm MMAD or multi-route mucosal exposures (oral, nasal, and ocular mucosal surfaces and intratracheal installation just above carina)	CXR; CT (CBCT); PET-CT	CXR: every sedation = pre-infection, D2, D4, D7, D11, D14, D2 CT: D0, D4, D11 (+18) PET-CT: D0, D4, D11 (+18)	CXR: radiologist interpretation PET: $SUV_{total\ lung}$, SUV_{max} LNs	CXR: mild unspecific infiltrates; CT: GGOs, thickened vessel structures, foci; PET: SUVmax in total lung and thoracic nodes	D2–D4; D4–D11; D4–D11	[9]

[a]Abbreviations: AGM, 'African green monkeys'; CBCT, conebeam CT, used in the MultiScan LFER 150 (Mediso Medical Imaging Systems); CEM, crab-eating (aka 'cynomolgus') macaques; CM, common marmosets; D, day (as in 'D2'); dpi, days post-infection; dpr, days post-re-exposure; EOP, end of experiment; f, female; HB, hamadryas baboons; LN, lymph node; LUS, lung ultrasound; m, male; MMAD, median mass aerodynamic diameter; p, passage; PFU, plaque-forming unit; RE, re-exposure; RM, rhesus monkeys; ROI, region of interest; SUVCMR, standard uptake value; cylinder-muscle ratio.
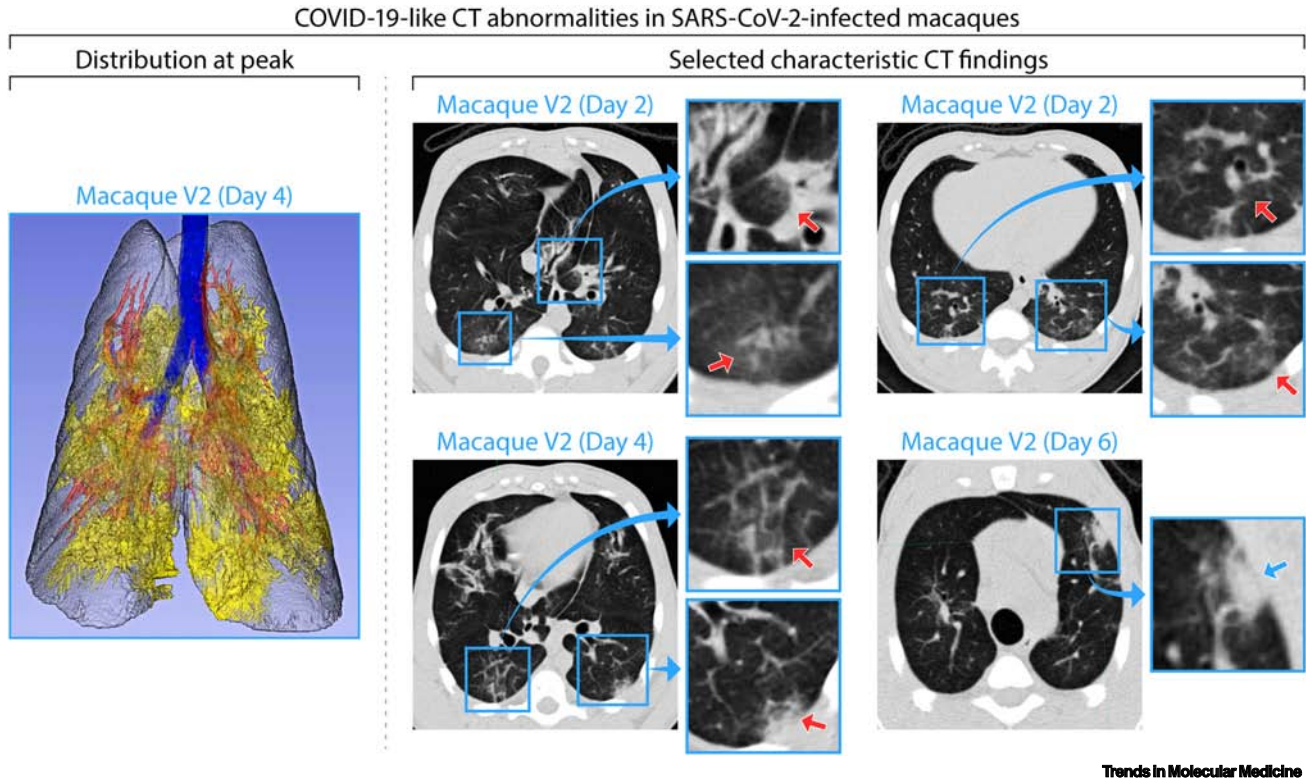
Figure 2. Common lung abnormalities detected by computed tomography (CT) of severe acute respiratory syndrome coronavirus 2 (SARS-CoV-2)-exposed macaques. Distribution of CT scan abnormalities in a 3D reconstruction image of a SARS-CoV-2-exposed macaque at peak disease, day 4 (left panel: blue, airways; gray, normal lung; red, vessels; yellow, imaging abnormalities). Selected characteristic abnormalities include: (i) peri-bronchial consolidation in the left accessory lobe (top-middle panel day 2: top inset, red arrow); (ii) posterior ground glass opacities (GGOs) with reticulation in the posterior right lung (top-middle panel day 2: bottom inset, red arrow); (iii) bilateral posterior GGOs with reticulation (top-right panel day 2: top and bottom insets, red arrows); (iv) GGOs with superimposed crazy-paving pattern (interlobular septal thickening) in right posterior lung (bottom-middle panel day 4: top inset, red arrow) and mixed GGOs with pleural-based consolidation in left posterior lung (bottom-middle panel day 4: bottom inset, red arrow); and (v) pleural-based mixed GGOs and consolidation (bottom-right panel day 6: inset, blue arrow). Adapted from [8]. Abbreviation: COVID-19, coronavirus disease 2019.

(e.g., GGOs, consolidation, crazy-paving pattern, and pleural thickening) have been developed to allow monitoring of disease progression by lung CT of NHPs (Table 1). These scores reflect the extent and longitudinal course of qualitative findings. However, poor scoring standardization across studies makes it challenging to compare experimental data from different research groups in detail outside the determination of a general pattern and peak. Recognizing that semiquantitative scoring relies on qualitative radiological assessments potentially subject to bias, several research groups have invested in the development of semiautomated, user-independent, quantitative readouts of radiographic abnormalities. For instance, normalized changes from pre-exposure baselines can be measured longitudinally as the **percent change in lung hyperdensity (PCLH)** [55] using CT data (Figure 4) [8,33]. Further development of such quantitative readouts should be encouraged.

A limited number of NHP studies have used PET-CT to measure ^{18}F-FDG uptake as a proxy for metabolic activity in the lungs and regional lymph nodes via anatomical co-registration with CT. Average, maximum, or peak (as robust alternative to maximum values, which could be affected by noise) **standard uptake values (SUVs)** in lung lesions, lymph nodes, or total lungs were used as measures of ^{18}F-FDG uptake and as surrogates of inflammatory activity. ^{18}F-FDG uptake was generally found to co-register with CT-identified structural abnormalities (e.g., GGOs and

Box 2. Other imaging techniques

Besides CXR, CT, and PET-CT, other imaging techniques are used for visualizing the lungs in NHPs exposed to SARS-CoV-2. In the clinic, ultrasound is commonly used for the diagnosis of pneumonia and to evaluate the integrity of the pleural space [37,108]. In COVID-19, ultrasound detected B-lines, consolidations, GGOs, and pleural thickening, and diagnostic accuracy was found to increase with disease severity [37,108]. However, the presence of air in non-lung parenchyma can impair the assessment of deeper parenchymal abnormalities [37], making it difficult to use this imaging modality to assess lung involvement in SARS-CoV-2-exposed NHPs. Additionally, interoperator and inter-reader variability makes standardization challenging. Thus far, ultrasound imaging has only been used in a single SARS-CoV-2-related NHP study, which concluded that ultrasound sensitivity to detect lung abnormalities was high, whereas the diagnostic efficacy for mild-to-moderate disease was relatively low [67]. With the drawbacks outweighing the advantages, ultrasound is not likely to gain traction in evaluating SARS-CoV-2-exposed NHPs.

Another often used clinical imaging modality is **magnetic resonance imaging (MRI)**. MRI has been used for evaluation of patients with COVID-19, primarily for examination of neurological complications. It is appealing for longitudinal imaging because of the lack of exposure to ionizing radiation. However, artifacts from cardiorespiratory motion and the intrinsically low MR signal of the lungs require dedicated sequences for lung evaluation. Although not the primary imaging modality of choice, the signs of interstitial pneumonia can nevertheless be detected by MRI [109,110]. The application of specific non-contrast- or contrast-enhanced MR sequences [111–114] has been investigated in clinical research settings (outside of infectious diseases) to provide free-breathing, high-resolution evaluation of lung anatomy and ventilation. Furthermore, hyperpolarized MRI using ^{129}Xe has been used to detect gas–blood exchange defects in patients with COVID-19 [115,116].

The last imaging modality discussed herein is a CT technique that differs from conventional CT, in which two data sets with different X-ray spectra are generated, called **dual-energy CT (DECT)**. DECT is a form of quantitative CT and has been used, with iodine as a contrast agent, in the evaluation of patients with COVID-19 to provide quantitative assessment of lung perfusion and detection of vascular abnormalities, including pulmonary embolism [117–121]. This technique was able to detect lung vascular impairment even in patients with asymptomatic COVID-19 [118], thereby holding promise for the evaluation of these parameters in the mild-to-moderate NHP model.

consolidation) during the course of the studies. Higher ^{18}F-FDG uptake was detected 2 days [8] or 4 days post-exposure [9] and resolved by day 11 or day 12 but increased again at later time points (up to day 35) [49]. Imaging from NHPs vaccinated against SARS-CoV-2 showed lower or no ^{18}F-FDG uptake in abnormalities within the lungs compared with unvaccinated control animals [50].

Challenges in applying medical imaging for the evaluation of SARS-CoV-2 infection in NHPs

Medical imaging of SARS-CoV-2-exposed NHPs is providing deeper insight into the pathophysiological processes related to lung abnormalities in patients with COVID-19. Indeed, the majority of clinical disease would be inapparent by clinical assessment (observation, physical examination, and laboratory blood markers), which justifies higher-resolution imaging evaluation. However, many challenges need to be overcome before noninvasive imaging readouts of the lungs can be reliably used as COVID-19 markers and to fully exploit their potential complement to standard immunological and virological assays. Some of these challenges are related to the NHP model. The clinical disease elicited by SARS-CoV-2 exposure in NHPs is generally mild to moderate (even radiographically), although some abnormalities associated with more severe disease (e.g., alveolar consolidation) have been reported occasionally [8,22,45,49,51,53,56–58]. Mild-to-moderate disease progression in NHPs mirrors that observed in humans (e.g., in the evolution of initial GGOs to organizing pneumonia and consolidation). Unsurprisingly, in (typically) young healthy animals without significant comorbidity, consistent radiographic abnormalities associated with **acute respiratory distress syndrome (ARDS)** in humans are absent, and the model has failed to assist in the evaluation of more serious lung pathology. Since COVID-19 severity in humans (and, therefore, also likelihood of hospitalization) has been associated with several risk factors, including advanced age and obesity [59], a handful of experiments used comorbid or aged NHPs to increase the likelihood of severe COVID-19 development. The few studies performed with aged NHPs [29,33,34,60–63] suggested
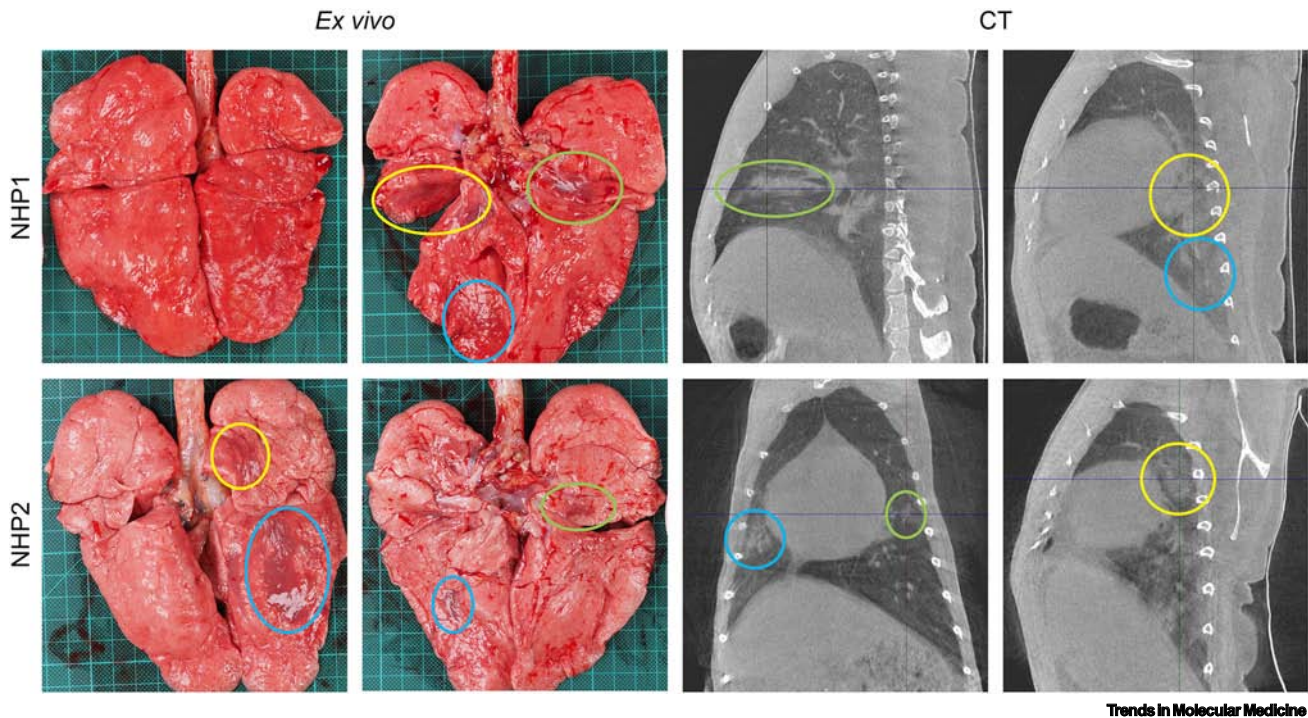
Figure 3. Lung abnormalities detected by computed tomography (CT) matched with gross pathology. Obtained just before euthanasia (day 7 post-exposure), these images were matched to gross pathology photographs. Lesions found reflecting the same location are marked with similarly colored circles. Adapted from [61]. Abbreviation: NHP, non-human primate.

that local inflammatory innate immune responses in the lungs are induced earlier than in younger NHPs and are responsible for protection against severe disease, although final outcomes were not significantly affected [33,60]. Similar to body mass index (BMI) in humans, obesity in NHPs is measured with a weight-for-height index (WHI). Values above 62 kg/m$^{2.7}$ and 67 kg/m^3 are indicative of obesity in crab-eating macaques and rhesus monkeys, respectively [64]. On average, these values correspond to body weights over 10 kg. Most NHPs used in SARS-CoV-2-related studies (Table 1) weighed less than 10 kg; therefore, the effect of obesity on NHP disease progression has yet to be addressed.

The SARS-CoV-2 exposure route may also be a factor influencing lung abnormality pattern and severity in NHPs. NHPs have been exposed to SARS-CoV-2 in various ways, most commonly via combined intranasal and intratracheal inoculation [12,22,27,35,49,50,53,54,56,57,65–67]. Multiple routes [9,13,16,20,23,26,28,29,31,33,34,46] lead to SARS-CoV-2 shedding. However, although infection is not necessarily dependent on respiratory tract exposure, it is plausible that the route of exposure impacts the progression of disease. Exposure deeper in the trachea was found to induce lung lesion development earlier compared with exposure in the upper trachea (Table 1) [9,49,54,56,65]. Small-particle aerosol exposure is an alternative to direct inoculation [9,32,34,44]. Overall, viral load, clinical disease progression and severity, plasma cytokine concentrations, and pathology are similar in aerosol-exposed NHPs compared with those exposed via other routes [34]. Since SARS-CoV-2 particles are ~100–120 nm in diameter, aerosols with droplet sizes of 1–3 µm have the potential to contain up to 120–460 virions per droplet [68]. The **half-maximum infection dose (ID$_{50}$)** of SARS-CoV-2 is unknown for both humans and NHPs but is likely to be less than 400 virions, which is the ID$_{50}$ of SARS-CoV [69]. These numbers
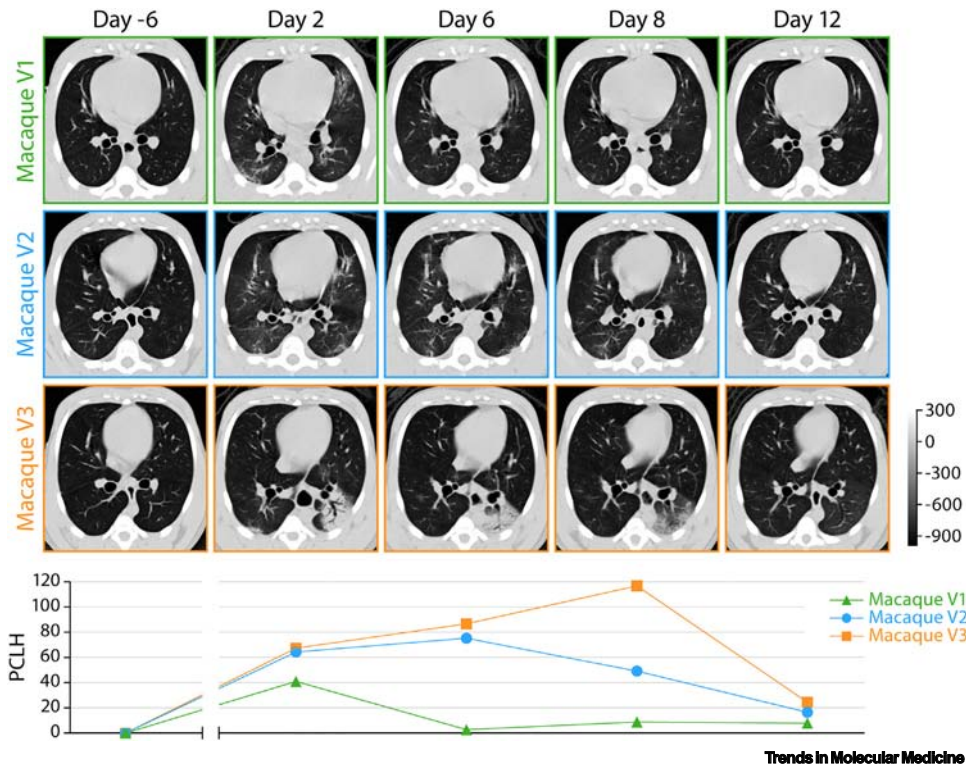
Figure 4. Data analysis of lung abnormalities detected by computed tomography (CT) of severe acute respiratory syndrome coronavirus 2 (SARS-CoV-2)-exposed macaques via percent change in lung hyperdensity (PCLH). Top: representative axial CT images in three SARS-CoV-2-exposed macaques for each indicated study day (D). The gray scale represents radiodensity in Hounsfield units (HU). Bottom: percentage change in volume of lung hyperdensity (PCLH) measured over time in the same SARS-CoV-2 inoculated macaques shown in the upper panel. Adapted from [8].

suggest that one droplet will suffice to initiate infection. Studies to determine the impact of aerosol particle size on the pulmonary disease phenotype (quality and quantity) are ongoing.

Other challenges are posed by the potential incompatibility of some experimental procedures with medical imaging experiments. For example, **bronchoalveolar lavage (BAL)** is often used to detect viruses and local immune responses in the lower respiratory tract [70,71]. In general, BAL and imaging should be concurrently used with caution, as BAL may produce CXR or CT imaging artifacts when performed on consecutive days [72], interfere with pulmonary pathogenesis (within-lung spread), and potentially confound histopathology. Of the 41 NHP SARS-CoV-2 studies examined, 24 used BAL during the infection phase and included imaging [12–16,20,22–24,27–30,33,35,50,51,53,54,56,65,73,74]. Eight included single BAL immediately before or at necropsy [12,20,22,33,54,57,65,73]. In one study, chest opacities and abnormalities might have been caused by the BAL procedure [12]. In two studies, BAL was deliberately not performed due to concerns of interference with imaging [8,49]. To guard against confounding findings due to BAL, medical imaging and necropsies should be performed on days not consecutive with BAL [72].

Additionally, incorporating quantitative, longitudinal medical imaging in high animal biosafety level (ABSL-3) or maximum containment settings (ABSL-4), as required for research with SARS-CoV-2 [75], is not without challenges, including increased experimental costs; medical imaging equipment

is not routinely available in most ABSL-3 and -4 settings; the maximum frequency of applied anesthesia required for imaging and the maximum number of NHPs that can practically be imaged at a single time point may create bottlenecks that limit optimal experimental design; and imaging conditions and technology vary among studies and sites, which makes it challenging to directly compare data obtained at separate sites (as highlighted herein). We foresee that advanced medical imaging of SARS-CoV-2-exposed NHPs may be enhanced by the development of best-practice principles and strategies to enable collaborative harmonization and standardization of data across studies, research groups, and organizations. Specific recommendations include choice of imaging modality (oriented to the appropriate scientific question), timing of evaluations, standardized data collection, centralized data repositories, and agreed-upon analysis approaches. Key principles, specific recommendations, and complex questions, based on the current knowledge of imaging NHPs focused on, although not solely applicable for, SARS-CoV-2 infection, are enumerated in Table 2 and the Outstanding questions section (see Outstanding questions).

Value of medical imaging, lessons from the clinic, and future directions

Although the absence of severe COVID-19 in the NHP model limits the translatability of imaging findings to some degree, medical imaging is established as a much-needed complementary readout to clinical, virological, or immunological assessments in the preclinical arena. Effectively modeling COVID-19 in NHPs, especially for non-fatal disease, requires meaningful measurements of infection and disease that include, but should not be limited to, viral quantification. In the absence of apparent clinical disease and viremia, RT-qPCR assessment of nasal and/or tracheal swab samples to measure viral load is often used as a proxy for disease severity. However, truly quantifiable measurements are challenging due to varying swab materials and quantities, sample site locations, RT-qPCR processes, and exposure routes, all of which may influence results [39]. Perhaps, the most important drawback is that SARS-CoV-2 infection involves the lower respiratory tract, which can only partly be sampled by invasive BALs. Furthermore, virological assessment alone cannot provide a complete picture of disease; indeed, histopathological and virological assessment of tissue (after necropsy) have both been required to

Table 2. Key principles and recommendations for imaging of SARS-CoV-2-exposed NHPs[a]

Topic	Key principles and recommendations
Modality	CXR: low sensitivity and reader dependence limits utility of CXR in a mild-to-moderate infection model LUS: high sensitivity, visibility of centrally located lesions is limited due to aeration, which limits its use in a mild-to-moderate infection model
	CT: recommended modality for detection of pulmonary abnormalities in SARS-CoV-2-exposed NHPs
	PET-CT: provides limited additional value for detection of lung abnormalities compared with CT (with ^{18}F-FDG), high value for functional characterization and quantification of LNs
Frequency and time	Obtain baseline image before infection
	Minimal imaging frequency after infection, one image in first 4 days post-exposure, one on day 5–10, and one on day 11–15.
	Imaging frequency can be reduced but not stopped at 14 days post-exposure
Analysis method	Qualitative evaluation of extent, distribution, type, and evolution of abnormality by expert readers is sufficient for general conclusion
	Quantitative analysis is preferred, preferably in automated and user-independent manner. In general, quantification of percentage of lung involvement, independent of type of abnormality, has been useful
Lung abnormality	Appearance of lung lesions should be correlated with gross pathology score but not necessarily RT-PCR values obtained from upper or lower respiratory tract sampling
	Other experimental procedures in lungs (e.g., BAL) can influence appearance of lung lesions during both imaging and necropsy

[a]Abbreviations: LN, lymph node; LUS, lung ultrasound.

describe the consequences of disease after infection, either at the organ/tissue or systemic level. Therefore, particularly in the lower respiratory tract, medical imaging of pulmonary disease contributes uniquely to the ability to understand and measure the consequences of infection [76]. Advanced medical imaging of the lungs of SARS-CoV-2-exposed NHPs shows promise in detecting and longitudinally evaluating disease. Without higher-resolution CT or PET-CT imaging, lung abnormalities reminiscent of COVID-19 (in character, distribution, location, and evolution; Figure 1) would not have been detected and could not have been assessed longitudinally in this model or matched with gross pathology (Figure 3). To fully exploit the potential of medical imaging in this setting, additional efforts should be devoted to correlate imaging results (on a per-lung or per-lobe basis) with histopathological abnormalities measured using quantitative scoring systems [16,60].

A limited number of human observational studies or clinical trials [77] have used medical imaging as part of the evaluation of both therapeutic and prophylactic treatment efficacy, including evaluations of tocilizumab (CT/CXR, qualitative) [78,79], favipiravir (CT, semiquantitative score), convalescent plasma (CT, qualitative) [80], and hydroxychloroquine versus febuxostat (CT, percent involvement) [81]. Generally, these have relied, at best, on semiquantitative CT scoring systems as secondary outcomes and often report only qualitative pre-/post-treatment changes. With regard to evaluation of MCMs in NHPs, a limited number of studies have been performed [82]. A recent study evaluating the efficacy of dalbavancin in rhesus monkeys resulted in fewer pulmonary infiltrates detectable by CXR in treated versus non-treated animals [83]. Other studies have instead relied on the characterization of CXR abnormalities using standard scoring systems. In the evaluation of remdesivir [20] and baricitinib [22] in rhesus monkeys, this approach was able to capture significant differences in lung involvement between treatment and control groups; however, in another study, no difference between groups could be observed by *in vivo* imaging despite detection of a treatment effect by lung pathology scores. An efficacy evaluation of hydroxychloroquine (either alone or in combination with azithromycin) in SARS-CoV-2-exposed crab-eating macaques used a semiquantitative CT score, compounding information on lesion type and volume, and found no evidence of antiviral activity or clinical benefit (as confirmed by recent meta-analyses) [56,84].

Recognizing that expert-generated qualitative or semiquantitative scoring systems (Figure 2) require dedicated personnel, need true blinding, and are intrinsically susceptible to bias, it is reasonable to foresee that current efforts in standardizing fully quantitative measures of lung disease, either by semiautomatic quantification of CT imaging abnormalities (e.g., longitudinally tracking the PCLH; Figure 4) or PET-CT abnormalities (e.g., tracking the SUV in specific regions of interest or globally), are likely to add value in forging host–virus–disease correlations and evaluating MCMs. In this evolving landscape, the ability to serially evaluate quantitative noninvasive (i.e., without serial euthanasia) measures of lung disease in a validated well-controlled experimental setting would significantly advance the evaluation of MCMs in these models. Furthermore, the large data sets derived from advanced imaging analyses have promise for the application of artificial intelligence (AI)-enabled machine-learning approaches as 'agnostic' evaluation of the fundamental relationship between infection and disease [85]. These are being explored in human clinical settings [86–91] but may be of higher yield in the controlled experimental settings afforded by animal modeling, including in uncovering findings otherwise unattainable with current readouts, such as in detecting subclinical organ involvement at unexpected sites for which pathological significance would be determined subsequently. Harmonization of scoring systems, or bidirectional/multidirectional exchange of CT images among research groups, and collaborations toward this end would likely move the field forward.

Clinician's corner

At present, NHP models of COVID-19 recapitulate only mild-to-moderate human disease.

While the development of an NHP model of severe COVID-19 is being pursued, current models highlight the added benefit of longitudinal medical imaging to characterize and quantify otherwise inapparent or mild clinical disease.

Thorough studies in NHP models and standardization of quantitative imaging readouts may shed light on COVID-19 lung pathophysiology beyond what can be learned in the clinical setting.

The application of novel imaging technologies in the preclinical arena may further enhance the value of noninvasive imaging in the assessment of COVID-19.

Although requiring the adaptation of dedicated settings or hardware to preclinical ABSL-3/4 imaging settings, these and other techniques that are gaining interest in the clinic (Box 2) may provide additional insight into the pathophysiology of lung involvement in COVID-19 and may be applied in NHPs.

In NHPs, PET-CT deploying radiotracers other than ^{18}F-FDG may provide additional insight into specific pathophysiological processes related to COVID-19 to fulfill more hallmarks of the ideal PET radiotracer for imaging inflammation, such as specificity and diagnostic value [92]. Some of these PET radiotracers have already been examined in small animal models of COVID-19, and studies in NHPs are ongoing. For example, [124]I-iodo-*N*,*N*-diethyl-2-5,7-dimethylpyrazolo [1,5-a]pyrimidine-3-acetamide (DPA-713), a radiotracer with **translocator protein (TSPO)** as a target selectively trapped by activated macrophages, was found to accumulate in pneumonic lesions in SARS-CoV-2-exposed golden hamsters [93]. The inflammation-specific peptide **DOTATATE** [paired with gallium-68 (^{68}Ga) or copper-64 (^{64}Cu)], a radiotracer with specificity for **somatostatin receptor 2 (SSTR2)**, was developed to improve the diagnosis of neuroendocrine tumors [94]. However, because SSTR2 is expressed by several inflammatory cells, DOTATATE is being investigated as a potential tracer for evaluation of several conditions, including cardiovascular [95] and infectious diseases [96], and appears to be particularly advantageous for imaging cardiac inflammation [92]. In one case report, DOTATATE was detected in an axillary lymph node after COVID-19 vaccination [97,98]. PET radiotracers targeted to the ACE2 receptor are also being developed [99]. Further in-depth studies investigating the expression levels of imaging target molecules in key cellular populations (e.g., macrophages) may prove invaluable in shaping the future landscape of PET-CT imaging in the context of COVID-19 [100].

Concluding remarks

Here, we have provided a detailed review of medical imaging in NHP models of COVID-19. Our search was limited to studies of medical imaging in SARS-CoV-2-exposed NHPs published online and found within online repositories. Several studies were limited in terms of sample size, data availability, and methodological quality, and the reported findings should be interpreted within that context. Nevertheless, these studies reflect current approaches. We argue that advanced imaging tools add unique insight into (so far) poorly understood relationships of SARS-CoV-2 exposure, infection, the host response, and disease presentation in the lungs. Challenges to advanced imaging characterization in NHP models require careful consideration and upstream investment that is likely well worth the return, not only in the current moment (for SARS-CoV-2/COVID-19), but also in the longer term for numerous respiratory viruses and diseases, known or as yet unencountered. Careful characterization of NHP models may enable exploration of complex determinants and progression of disease (see Outstanding questions). Advanced medical imaging of adequate resolution is vital to truly characterize (quality) and reliably measure (quantity) disease without bias to understand and provide meaningful longitudinal readouts of disease (in animal studies) and bridge to humans; thus, medical imaging will be an increasingly important component of the NHP modelers' toolkit.

^{18}F-FDG for PET-CT of the lungs, for example, toward visualization of the effective or pathological host immune response?

Author contributions

Declaration of interests

The authors declare no competing interests.

References

1. Rubin, G.D. *et al.* (2020) The role of chest imaging in patient management during the COVID-19 pandemic: a multinational consensus statement from the Fleischner Society. *Radiology* 296, 172–180
2. Pan, F. *et al.* (2020) Time course of lung changes at chest CT during recovery from coronavirus disease 2019 (COVID-19). *Radiology* 295, 715–721
3. Ai, T. *et al.* (2020) Correlation of chest CT and RT-PCR testing for coronavirus disease 2019 (COVID-19) in China: a report of 1014 cases. *Radiology* 296, E32–E40
4. Cleary, S.J. *et al.* (2020) Animal models of mechanisms of SARS-CoV-2 infection and COVID-19 pathology. *Br. J. Pharmacol.* 177, 4851–4865
5. Zamorano Cuervo, N. and Grandvaux, N. (2020) ACE2: evidence of role as entry receptor for SARS-CoV-2 and implications in comorbidities. *eLife* 9, e61390
6. Muñoz-Fontela, C. *et al.* (2020) Animal models for COVID-19. *Nature* 586, 509–515
7. Zeiss, C.J. *et al.* (2021) Animal models of COVID-19. I. Comparative virology and disease pathogenesis. *ILAR J.* Published online April 9, 2021. https://doi.org/10.1093/ilar/ilab007
8. Finch, C.L. *et al.* (2020) Characteristic and quantifiable COVID-19-like abnormalities in CT- and PET/CT-imaged lungs of SARS-CoV-2-infected crab-eating macaques (*Macaca fascicularis*). *bioRxiv* Published online May 14, 2020. https://doi.org/10.1101/2020.05.14.096727
9. Hartman, A.L. *et al.* (2020) SARS-CoV-2 infection of African green monkeys results in mild respiratory disease discernible by PET/CT imaging and shedding of infectious virus from both respiratory and gastrointestinal tracts. *PLoS Pathog.* 16, e1008903
10. Simpson, S. *et al.* (2020) Radiological Society of North America expert consensus statement on reporting chest CT findings related to COVID-19. Endorsed by the Society of Thoracic Radiology, the American College of Radiology, and RSNA - secondary publication. *J. Thorac. Imaging* 35, 219–227
11. Simpson, S. *et al.* (2020) Radiological Society of North America expert consensus document on reporting chest CT findings related to COVID-19: endorsed by the Society of Thoracic Radiology, the American College of Radiology, and RSNA. *Radiol. Cardiothorac. Imaging* 2, e200152
12. Woolsey, C. *et al.* (2021) Establishment of an African green monkey model for COVID-19 and protection against re-infection. *Nat. Immunol.* 22, 86–98
13. Speranza, E. *et al.* (2021) Single-cell RNA sequencing reveals SARS-CoV-2 infection dynamics in lungs of African green monkeys. *Sci. Transl. Med.* 13, eabe8146
14. Rosenke, K. *et al.* (2021) UK B.1.1.7 (Alpha) variant exhibits increased respiratory replication and shedding in nonhuman primates. *Emerg. Microbes Infect.* 10, 2173–2182
15. Frueh, F.W. *et al.* (2021) An orally available cathepsin L inhibitor protects lungs against SARS-CoV-2-induced diffuse alveolar damage in African green monkeys. *bioRxiv* Published online July 21, 2021. https://doi.org/10.1101/2021.07.20.453127
16. Munster, V.J. *et al.* (2020) Respiratory disease in rhesus macaques inoculated with SARS-CoV-2. *Nature* 585, 268–272
17. Shan, C. *et al.* (2020) Infection with novel coronavirus (SARS-CoV-2) causes pneumonia in *Rhesus macaques*. *Cell Res.* 30, 670–677
18. Deng, W. *et al.* (2020) Primary exposure to SARS-CoV-2 protects against reinfection in rhesus macaques. *Science* 369, 818–823
19. Yu, P. *et al.* (2020) Age-related rhesus macaque models of COVID-19. *Anim. Model Exp. Med.* 3, 93–97
20. Williamson, B.N. *et al.* (2020) Clinical benefit of remdesivir in rhesus macaques infected with SARS-CoV-2. *Nature* 585, 273–276
21. Deng, W. *et al.* (2020) Ocular conjunctival inoculation of SARS-CoV-2 can cause mild COVID-19 in rhesus macaques. *Nat. Commun.* 11, 4400
22. Hoang, T.N. *et al.* (2021) Baricitinib treatment resolves lower-airway macrophage inflammation and neutrophil recruitment in SARS-CoV-2-infected rhesus macaques. *Cell* 184, 460–475 e421
23. Furuyama, W. *et al.* (2021) Rapid protection from COVID-19 in nonhuman primates vaccinated intramuscularly but not intranasally with a single dose of a recombinant vaccine. *bioRxiv* Published online January 19, 2021. https://doi.org/10.1101/2021.01.19.426885
24. Hassan, A.O. *et al.* (2021) A single intranasal dose of chimpanzee adenovirus-vectored vaccine protects against SARS-CoV-2 infection in rhesus macaques. *Cell Rep. Med.* 2, 100230
25. Gu, C. *et al.* (2021) A human antibody of potent efficacy against SARS-CoV-2 in rhesus macaques showed strong blocking activity to B.1.351. *mAbs* 13, 1930636
26. Jiao, L. *et al.* (2021) The gastrointestinal tract is an alternative route for SARS-CoV-2 infection in a nonhuman primate model. *Gastroenterology* 160, 1647–1661
27. Van Rompay, K.K.A. *et al.* (2021) Early post-infection treatment of SARS-CoV-2 infected macaques with human convalescent plasma with high neutralizing activity reduces lung inflammation. *bioRxiv* Published online September 1, 2021. https://doi.org/10.1101/2021.09.01.458520
28. Pillet, S. *et al.* (2021) Safety, immunogenicity and protection provided by unadjuvanted and adjuvanted formulations of recombinant plant-derived virus-like particle vaccine candidate for COVID-19 in non-human primates. *bioRxiv* Published online May 15, 2021. https://doi.org/10.1101/2021.05.15.444262
29. Speranza, E. *et al.* (2021) Age-related differences in immune dynamics during SARS-CoV-2 infection in rhesus macaques.

bioRxiv Published online September 8, 2021. https://doi.org/10.1101/2021.09.08.459430

30. Melton, A. *et al.* (2021) The pigtail macaque (*Macaca nemestrina*) model of COVID-19 reproduces diverse clinical outcomes and reveals new and complex signatures of disease. *bioRxiv* Published online August 30, 2021. https://doi.org/10.1101/2021.08.28.458047

31. Lu, S. *et al.* (2020) Comparison of nonhuman primates identified the suitable model for COVID-19. *Signal Transduct. Target Ther.* 5, 157

32. Johnston, S.C. *et al.* (2021) Development of a coronavirus disease 2019 nonhuman primate model using airborne exposure. *PLoS ONE* 16, e0246366

33. Singh, D.K. *et al.* (2021) Responses to acute infection with SARS-CoV-2 in the lungs of rhesus macaques, baboons and marmosets. *Nat. Microbiol.* 6, 73–86

34. Blair, R.V. *et al.* (2021) Acute respiratory distress in aged, SARS-CoV-2-infected African green monkeys but not rhesus macaques. *Am. J. Pathol.* 191, 274–282

35. Vogel, A.B. *et al.* (2021) BNT162b vaccines protect rhesus macaques from SARS-CoV-2. *Nature* 592, 283–289

36. Fusco, R. *et al.* (2021) Artificial intelligence and COVID-19 using chest CT scan and chest X-ray images: machine learning and deep learning approaches for diagnosis and treatment. *J. Pers. Med.* 11, 993

37. Aljondi, R. and Alghamdi, S. (2020) Diagnostic value of imaging modalities for COVID-19: scoping review. *J. Med. Internet Res.* 22, e19673

38. Durrani, M. *et al.* (2020) Chest X-rays findings in COVID 19 patients at a University Teaching Hospital - a descriptive study. *Pak. J. Med. Sci.* 36, S22–S26

39. Kwee, T.C. and Kwee, R.M. (2020) Chest CT in COVID-19: what the radiologist needs to know. *Radiographics* 40, 1848–1865

40. Xu, B. *et al.* (2020) Chest CT for detecting COVID-19: a systematic review and meta-analysis of diagnostic accuracy. *Eur. Radiol.* 30, 5720–5727

41. De Smet, K. *et al.* (2021) Diagnostic performance of chest CT for SARS-CoV-2 infection in individuals with or without COVID-19 symptoms. *Radiology* 298, E30–E37

42. Kim, H. *et al.* (2020) Diagnostic performance of CT and reverse transcriptase polymerase chain reaction for coronavirus disease 2019: a meta-analysis. *Radiology* 296, E145–E155

43. Khatami, F. *et al.* (2020) A meta-analysis of accuracy and sensitivity of chest CT and RT-PCR in COVID-19 diagnosis. *Sci. Rep.* 10, 22402

44. Bixler, S.L. *et al.* (2021) Aerosol exposure of cynomolgus macaques to SARS-CoV-2 results in more severe pathology than existing models. *bioRxiv* Published online April 27. 2021. https://doi.org/10.1101/2021.04.27.441510

45. Harris, P.E. *et al.* (2021) A synthetic peptide CTL vaccine targeting nucleocapsid confers protection from SARS-CoV-2 challenge in rhesus macaques. *Vaccines (Basel)* 9, 520

46. Kobiyama, K. *et al.* (2021) Optimization of an LNP-mRNA vaccine candidate targeting SARS-CoV-2 receptor-binding domain. *bioRxiv* Published online March 4, 2021. https://doi.org/10.1101/2021.03.04.433852

47. Ye, Z. *et al.* (2020) Chest CT manifestations of new coronavirus disease 2019 (COVID-19): a pictorial review. *Eur. Radiol.* 30, 4381–4389

48. Kovács, A. *et al.* (2021) The sensitivity and specificity of chest CT in the diagnosis of COVID-19. *Eur. Radiol.* 31, 2819–2824

49. Böszörményi, K.P. *et al.* (2021) The post-acute phase of SARS-CoV-2 infection in two macaques species is associated with signs of ongoing virus replication and pathology in pulmonary and extrapulmonary tissues. *Viruses* 13, 1673

50. Arunachalam, P.S. *et al.* (2021) Adjuvanting a subunit COVID-19 vaccine to induce protective immunity. *Nature* 594, 253–258

51. Zabaleta, N. *et al.* (2021) An AAV-based, room-temperature-stable, single-dose COVID-19 vaccine provides durable immunogenicity and protection in non-human primates. *Cell Host Microbe* 29, 1437–1453

52. White, A.G. *et al.* (2017) Analysis of ^{18}FDG PET/CT imaging as a tool for studying *Mycobacterium tuberculosis* infection and treatment in non-human primates. *J. Vis. Exp.* 127, 56375

53. Maisonnasse, P. *et al.* (2021) COVA1-18 neutralizing antibody protects against SARS-CoV-2 in three preclinical models. *Nat. Commun.* 12, 6097

54. Rauch, S. *et al.* (2020) mRNA vaccine CVnCoV protects non-human primates from SARS-CoV-2 challenge infection. *bioRxiv* Published online December 23, 2020. https://doi.org/10.1101/2020.12.23.424138

55. Solomon, J. *et al.* (2014) New image analysis technique for quantitative longitudinal assessment of lung pathology on CT in infected rhesus macaques. In *2014 IEEE 27th International Symposium on Computer-Based Medical Systems*, pp. 169–172, IEEE

56. Maisonnasse, P. *et al.* (2020) Hydroxychloroquine use against SARS-CoV-2 infection in non-human primates. *Nature* 585, 584–587

57. Bewley, K.R. *et al.* (2021) Immunological and pathological outcomes of SARS-CoV-2 challenge following formalin-inactivated vaccine in ferrets and rhesus macaques. *Sci. Adv.* 7, eabg7996

58. Ehaideb, S.N. *et al.* (2020) Evidence of a wide gap between COVID-19 in humans and animal models: a systematic review. *Crit. Care* 24, 594

59. Halpern, B. *et al.* (2021) Obesity and COVID-19 in Latin America: a tragedy of two pandemics - official document of the Latin American Federation of Obesity Societies. *Obes. Rev.* 22, e13165

60. Rockx, B. *et al.* (2020) Comparative pathogenesis of COVID-19, MERS, and SARS in a nonhuman primate model. *Science* 368, 1012–1015

61. Solforosi, L. *et al.* (2021) Immunogenicity and efficacy of one and two doses of Ad26.COV2.S COVID vaccine in adult and aged NHP. *J. Exp. Med.* 218, e20202756

62. Gallo Marin, B. *et al.* (2021) Predictors of COVID-19 severity: a literature review. *Rev. Med. Virol.* 31, 1–10

63. Verity, R. *et al.* (2020) Estimates of the severity of coronavirus disease 2019: a model-based analysis. *Lancet Infect. Dis.* 20, 669–677

64. Sterck, E.H.M. *et al.* (2019) Determining overweight and underweight with a new weight-for-height index in captive group-housed macaques. *Am. J. Primatol.* 81, e22996

65. Salguero, F.J. *et al.* (2021) Comparison of rhesus and cynomolgus macaques as an infection model for COVID-19. *Nat. Commun.* 12, 1260

66. Urano, E. *et al.* (2021) COVID-19 cynomolgus macaque model reflecting human COVID-19 pathological conditions. *Proc. Natl. Acad. Sci. U. S. A.* 118, e2104847118

67. Schilp, C.M. *et al.* (2021) A comparative study of chest CT with lung ultrasound after SARS-CoV-2 infection in the assessment of pulmonary lesions in rhesus monkeys (*Macaca mulatta*). *Front. Vet. Sci.* 8, 748635

68. Bar-On, Y.M. *et al.* (2020) SARS-CoV-2 (COVID-19) by the numbers. *eLife* 9, e57309

69. Watanabe, T. *et al.* (2010) Development of a dose-response model for SARS coronavirus. *Risk Anal.* 30, 1129–1138

70. Lim, S. *et al.* (2018) Bronchoalveolar lavage affects computed tomographic and radiographic characteristics of the lungs in healthy dogs. *Vet. Radiol. Ultrasound* 59, 564–570

71. Gabe, L.M. *et al.* (2011) Effect of segmental bronchoalveolar lavage on quantitative computed tomography of the lung. *Acad. Radiol.* 18, 876–884

72. Maaskant, A. *et al.* (2021) Bronchoalveolar lavage affects thorax computed tomography of healthy and SARS-CoV-2 infected rhesus macaques (*Macaca mulatta*). *PLoS ONE* 16, e0252941

73. Gooch, K.E. *et al.* (2021) One or two dose regimen of the SARS-CoV-2 synthetic DNA vaccine INO-4800 protects against respiratory tract disease burden in nonhuman primate challenge model. *Vaccine* 39, 4885–4894

74. Sulbaran, G. *et al.* (2021) Immunization with synthetic SARS-CoV-2 S glycoprotein virus-like particles protects Macaques from infection. *bioRxiv* Published online July 26, 2021. https://doi.org/10.1101/2021.07.26.453755

75. CDC (2021) *Interim Laboratory Biosafety Guidelines for Handling and Processing Specimens Associated With Coronavirus Disease 2019 (COVID-19)*, CDC

76. Vannucci, J. *et al.* (2020) Usefulness of bronchoalveolar lavage in suspect COVID-19 repeatedly negative swab test and interstitial lung disease. *J. Glob. Antimicrob. Resist.* 23, 67–69

77. Saleki, K. *et al.* (2021) Interferon therapy in patients with SARS, MERS, and COVID-19: a systematic review and meta-analysis of clinical studies. *Eur. J. Pharmacol.* 906, 174248

78. Dastan, F. *et al.* (2020) Promising effects of tocilizumab in COVID-19: a non-controlled, prospective clinical trial. *Int. Immunopharmacol.* 88, 106869

79. Masci, G.M. *et al.* (2021) Tocilizumab effects in COVID-19 pneumonia: role of CT texture analysis in quantitative assessment of response to therapy. *Radiol. Med.* 126, 1170–1180

80. Zeng, H. *et al.* (2020) The efficacy assessment of convalescent plasma therapy for COVID-19 patients: a multi-center case series. *Signal Transduct. Target Ther.* 5, 219

81. Davoodi, L. *et al.* (2020) Febuxostat therapy in outpatients with suspected COVID-19: a clinical trial. *Int. J. Clin. Pract.* 74, e13600

82. Cai, Q. *et al.* (2020) Experimental treatment with favipiravir for COVID-19: an open-label control study. *Engineering (Beijing)* 6, 1192–1198

83. Wang, G. *et al.* (2021) Dalbavancin binds ACE2 to block its interaction with SARS-CoV-2 spike protein and is effective in inhibiting SARS-CoV-2 infection in animal models. *Cell Res.* 31, 17–24

84. Amani, B. *et al.* (2021) Hydroxychloroquine plus standard of care compared with standard of care alone in COVID-19: a meta-analysis of randomized controlled trials. *Sci. Rep.* 11, 11974

85. Deng, H. and Li, X. (2021) AI-empowered computational examination of chest imaging for COVID-19 treatment: a review. *Front. Artif. Intell.* 4, 612914

86. Pan, F. *et al.* (2021) A novel deep learning-based quantification of serial chest computed tomography in coronavirus disease 2019 (COVID-19). *Sci. Rep.* 11, 417

87. Lassau, N. *et al.* (2021) Integrating deep learning CT-scan model, biological and clinical variables to predict severity of COVID-19 patients. *Nat. Commun.* 12, 634

88. Zhang, X. *et al.* (2021) A deep learning integrated radiomics model for identification of coronavirus disease 2019 using computed tomography. *Sci. Rep.* 11, 3938

89. Tan, H.-B. *et al.* (2020) The study of automatic machine learning base on radiomics of non-focus area in the first chest CT of different clinical types of COVID-19 pneumonia. *Sci. Rep.* 10, 18926

90. Wang, X. *et al.* (2021) Correlation between lung infection severity and clinical laboratory indicators in patients with COVID-19: a cross-sectional study based on machine learning. *BMC Infect. Dis.* 21, 192

91. Xiong, F. *et al.* (2021) The clinical classification of patients with COVID-19 pneumonia was predicted by Radiomics using chest CT. *Medicine (Baltimore)* 100, e25307

92. Iking, J. *et al.* (2021) Imaging inflammation with positron emission tomography. *Biomedicines* 9, 212

93. Ruiz-Bedoya, C.A. *et al.* (2021) ^{124}I-Iodo-DPA-713 positron emission tomography in a hamster model of SARS-CoV-2 infection. *Mol. Imaging Biol.* Published online August 23, 2021. https://doi.org/10.1007/s11307-021-01638-5

94. Papadakis, G.Z. *et al.* (2021) Current status and future prospects of PET-imaging applications in patients with gastro-entero-pancreatic neuroendocrine tumors (GEP-NETs). *Eur. J. Radiol.* 143, 109932

95. Tarkin, J.M. *et al.* (2017) Detection of atherosclerotic inflammation by ^{68}Ga-DOTATATE PET compared to FDG PET imaging. *J. Am. Coll. Cardiol.* 69, 1774–1791

96. Skovsbo Clausen, A. *et al.* (2020) ^{64}Cu-DOTATATE positron emission tomography (PET) of *Borrelia burgdorferi* infection: *in vivo* imaging of macrophages in experimental model of Lyme arthritis. *Diagnostics (Basel)* 10, 790

97. Brophy, J. *et al.* (2021) DOTATATE uptake in an axillary lymph node after COVID-19 vaccination. *Clin. Nucl. Med.* Published online July 14, 2021. https://doi.org/10.1097/RLU.0000000000003847

98. Surasi, D.S.S. *et al.* (2021) Supraclavicular and axillary lymphadenopathy induced by COVID-19 vaccination on ^{18}F-fluorthanatrace, ^{68}Ga-DOTATATE, and ^{18}F-fluciclovine PET/CT. *Clin. Nucl. Med.* Published online September 8, 2021. https://doi.org/10.1097/RLU.0000000000003891

99. Zhu, H. *et al.* (2021) Molecular PET/CT profiling of ACE2 expression in vivo: implications for infection and outcome from SARS-CoV-2. *Adv. Sci. (Weinh)* 8, e2100965

100. Lee, H. *et al.* (2021) Discovery of potential imaging and therapeutic targets for severe inflammation in COVID-19 patients. *Sci. Rep.* 11, 14151

101. V'kovski, P. *et al.* (2021) Coronavirus biology and replication: implications for SARS-CoV-2. *Nat. Rev. Microbiol.* 19, 155–170

102. Wong, D.W.L. *et al.* (2021) Multisystemic cellular tropism of SARS-CoV-2 in autopsies of COVID-19 patients. *Cells* 10, 1900

103. Chandrashekar, A. *et al.* (2020) SARS-CoV-2 infection protects against rechallenge in rhesus macaques. *Science* 369, 812–817

104. Gao, Q. *et al.* (2020) Development of an inactivated vaccine candidate for SARS-CoV-2. *Science* 369, 77–81

105. Munster, V.J. *et al.* (2020) Respiratory disease and virus shedding in rhesus macaques inoculated with SARS-CoV-2. *bioRxiv* Published online March 21, 2020. https://doi.org/10.1101/2020.03.21.001628

106. van Doremalen, N. *et al.* (2020) ChAdOx1 nCoV-19 vaccination prevents SARS-CoV-2 pneumonia in rhesus macaques. *Nature* 586, 578–582

107. Yu, J. *et al.* (2020) DNA vaccine protection against SARS-CoV-2 in rhesus macaques. *Science* 369, 806–811

108. Shammus, R. *et al.* (2020) The role of imaging and other diagnostic approaches in COVID-19. *Acta Biomed.* 91, e2020019

109. Di Girolamo, M. *et al.* (2020) An incidental diagnosis of SARS-CoV-2 pneumonia with magnetic resonance imaging. *Cureus* 12, e12115

110. Kumar, H. *et al.* (2021) Discrepancies in the clinical and radiological profiles of COVID-19: a case-based discussion and review of literature. *World J. Radiol.* 13, 75–93

111. Chen, L. *et al.* (2020) Improving dynamic contrast-enhanced MRI of the lung using motion-weighted sparse reconstruction: initial experiences in patients. *Magn. Reson. Imaging* 68, 36–44

112. Chen, L. *et al.* (2019) A study of the correlation of perfusion parameters in high-resolution GRASP MRI with microvascular density in lung cancer. *J. Magn. Reson. Imaging* 49, 1186–1194

113. Feng, L. *et al.* (2019) Simultaneous evaluation of lung anatomy and ventilation using 4D respiratory-motion-resolved ultrashort echo time sparse MRI. *J. Magn. Reson. Imaging* 49, 411–422

114. Chen, L. *et al.* (2018) Free-breathing dynamic contrast-enhanced MRI for assessment of pulmonary lesions using golden-angle radial sparse parallel imaging. *J. Magn. Reson. Imaging* 48, 459–468

115. Grist, J.T. *et al.* (2021) Hyperpolarized ^{129}Xe MRI abnormalities in dyspneic patients 3 months after COVID-19 pneumonia: preliminary results. *Radiology* 301, E353–E360

116. Li, H. *et al.* (2021) Damaged lung gas exchange function of discharged COVID-19 patients detected by hyperpolarized ^{129}Xe MRI. *Sci. Adv.* 7, eabc8180

117. Poschenrieder, F. *et al.* (2021) Severe COVID-19 pneumonia: perfusion analysis in correlation with pulmonary embolism and vessel enlargement using dual-energy CT data. *PLoS ONE* 16, e0252478

118. Nagpal, P. *et al.* (1985) (2021) Case studies in physiology: temporal variations of the lung parenchyma and vasculature in asymptomatic COVID-19 pneumonia: a multispectral CT assessment. *J. Appl. Physiol.* 131, 454–463

119. Remy-Jardin, M. *et al.* (2021) Assessment of pulmonary arterial circulation 3 months after hospitalization for SARS-CoV-2 pneumonia: dual-energy CT (DECT) angiographic study in 55 patients. *EClinicalMedicine* 34, 100778

120. Ridge, C.A. *et al.* (2020) Dual-energy CT pulmonary angiography (DECTPA) quantifies vasculopathy in severe COVID-19 pneumonia. *Radiol. Cardiothorac. Imaging* 2, e200428

121. Nagpal, P. *et al.* (2021) Quantitative CT imaging and advanced visualization methods: potential application in novel coronavirus disease 2019 (COVID-19) pneumonia. *BJR Open* 3, 20200043

122. Arunachalam, P.S. (2021) Adjuvanting a subunit SARS-CoV-2 nanoparticle vaccine to induce protective immunity in non-human primates. *bioRxiv* Published online February 11, 2021. https://doi.org/10.1101/2021.02.10.430696